International Journal of Minerals, Metallurgy and Materials
Volume 26, Number 8, August 2019, Page 1020
https://doi.org/10.1007/s12613-019-1805-x

Crystalline texture evolution, control of the tribocorrosion behavior, and significant enhancement of the abrasion properties of a Ni–P nanocomposite coating enhanced by zirconia nanoparticles

Masoud Sabzi[1)], *Saeid Mersagh Dezfuli*[2)], *and Zohre Balak*[3)]

1) Young Researchers and Elite Club, Dezful Branch, Islamic Azad University, Dezful 6461645165, Iran

2) Department of Materials Science and Engineering, Science and Research Branch, Islamic Azad University, Tehran 1477893855, Iran

3) Department of Materials Science, Islamic Azad University, Ahwaz 6224927333, Iran

(Received: 9 July 2018; revised: 30 January 2019; accepted: 12 February 2019)

Abstract: This paper describes an investigation of the effect of ZrO_2 nanoparticles on the abrasive properties, crystalline texture developments, and tribocorrosion behavior of Ni–P nanostructured coatings. In the investigation, Ni–P and Ni–P–ZrO_2 nanostructured coatings are deposited on St52 steel via the electroless method. Transmission electron microscopy (TEM), field emission scanning electron microscopy (FE-SEM), X-ray diffraction (XRD), energy dispersive spectroscopy (EDS), cyclic-static polarization tests in 3.5wt% NaCl solution, the tribocorrosion test (by back-and-forth wear in electrochemical cell), and the microhardness test using the Vickers method were performed to characterize and analyze the deposited coatings. The results of this study showed that the addition of ZrO_2 nanoparticles to the Ni–P electroless bath produced the following: a sharp increase in wear and hardness resistance, the change of the wear mechanism from sheet to adhesive mode, the reduction of pitting corrosion resistance, significant reduction in the tribocorrosion protective properties, change in the preferred orientation of the crystalline texture coating from (111) to (200), increase in the sedimentation rate during the deposit process, and a sharp increase in the thickness of the Ni–P nanostructured coatings.

Keywords: Ni–P nanocomposite coatings; ZrO_2 nanoparticles; crystalline texture; corrosion resistance; abrasive properties; tribocorrosion behavior

1. Introduction

Since the nineteenth century, nickel-based coatings produced by electroplating have been used for increased corrosion and wear resistance as well as decorative applications. The electroless plating process was introduced as a new plating method by Riedel in 1946. A nickel-based coating produced using the electroless plating method is a coating that has a relatively good performance under different corrosion and abrasion conditions. These properties are strongly influenced by the conditions of the plating bath and the weight percent of the deposited reinforcement particles [1–3]. One of the special applications of nickel electroless coatings is in the oil industry, in which the coatings are subject to catastrophic abrasion and corrosion conditions [4–6]. In one study, Zielińska *et al.* [7] studied the effect of surfactants on the electroless deposition of Ni–P–nano-ZrO_2 composite coatings. The results of these investigations showed that the presence of surfactants in the electroless bath increases the absorption of zirconia nanoparticles in the Ni–P–nano-ZrO_2 composite coating. In other studies [8–9], researchers reported that increasing the amount of nanoparticles of ZrO_2 in the electrolyte bath resulted in a decrease in phosphorus concentration in Ni–P–ZrO_2 coatings.

Wear and corrosion are the most important mechanisms of material degradation in industry. Addressing such material degradation imposes a high cost per year in different industries. Tribocorrosion is a term that expresses the state of destruction of material as a result of the combination of tri-

Corresponding author: Saeid Mersagh Dezfuli E-mail: saeed.m.dezfooli@gmail.com

bological (wear) and chemical-electrochemical (corrosion) processes [9–10]. When the corrosion and abrasion conditions prevail, the damage will be greatly increased compared to situations where only one of them is the cause of the destruction. The tribocorrosion test examines the effects of corrosion on abrasion and vice versa (i.e., the wear effects on corrosion). So far, extensive studies have been conducted to investigate the effects of synchronization of corrosion and abrasion. However, because of the complexity involved, there are still many unknown fields in this area. Surface properties, type of passive film, and its physical and mechanical properties have major effects on the amount of surface mechanical wear. Alternatively, abrasive pairs, the friction coefficient, as well as the created wear rate and type can also affect surface corrosion [11–13]. Unlike most studies conducted on the corrosion behavior of coatings and passive metals that have focused on uniform corrosion conditions, a small number of studies have investigated the tribocorrosion behavior of metals in localized corrosion conditions [14–15].

Nickel-phosphorus electroless coating is one of the most commonly used coatings in corrosive and abrasive environments. Nickel-phosphorus electroless coating with high phosphorus percentages in crude conditions has shown good corrosion resistance because of its amorphous structure and the formation of the persistent passive film in corrosive environments. This passive layer is based on phosphate compounds and increases the corrosion resistance by blocking the cavities of the coating [16–17]. However, note that the thermal treatment of nickel–phosphor electroless coating reduces the corrosion resistance of the coating via the formation of nickel crystalline structure and the Ni_3P secondary phase. Alternatively, changing the amorphous structure of the nickel–phosphor coating to the nanocrystalline structure as well as the created phase changes influence the heat treatment, resulting in an increase in the hardness and the wear resistance of this coating [18–19]. An optimal form of corrosion and abrasion resistance can be created in Ni–P coatings by choosing the appropriate temperature for the heat treatment.

Undoubtedly, the use of composite coatings improves the corrosion properties of metals and alloys [20–21]. Although many studies have been conducted on the wear and corrosion behavior of nickel–phosphorus electroless coatings in recent years [18–19,22], the effect of the synchronization of these two phenomena has not yet been evaluated. Accordingly, the effects of ZrO_2 ceramic nanoparticles on the abrasive properties, crystalline texture developments, and tribocorrosion behavior of Ni–P nanostructured coatings were investigated in this study.

2. Experimental

In this study, Ni–P and Ni–P–ZrO_2 nanostructured coatings were deposited on a St52 steel substrate using electroless plating. For this purpose, St52 steel substrates were prepared as disk-shaped samples with a diameter of 5 cm and a thickness of 10 mm. Surface preparation of the samples includes grinding up to 1000 mesh, decreasing in a NaOH alkaline solution at 80°C, washing in acetone in an ultrasonic bath, followed by alternative washing with distilled water. MacDermid ELV 811 commercial solution was used as an electroless solution. This solution contains 60 g/L of nickel sulfate, 30 g/L of sodium hypophosphite, and good amounts of additive and stabilizing agent. ZrO_2 nanoparticles were used in 8 g/L electroless baths as reinforcement particles in the deposited nanostructured coatings. The nanoparticles were analyzed via TEM (a CM120 model, manufactured by Philips Netherlands) and XRD (an X'Pert PRO MP model, manufactured by the Netherlands PANalytical Company). The chemical composition of St52 steel used in this study was investigated by the Spark emission spectrometer made in Germany; the results of the study are reported in Table 1.

Table 1. Chemical composition of St52 steel used in this study

wt%

C	Mn	Si	Cr	Ni	Cu	P	Fe
0.19	1.24	0.49	0.28	0.51	0.29	0.03	Bal.

The plating process was conducted in a double-sided bath with the capacity of 400 mL that was connected to the circulating water heating system. Note that the deposition process was conducted at 50°C and pH = 4.5 ± 0.1 for 4 h to achieve a coating with approximately 40 μm thickness. After depositing the Ni–P and Ni–P–ZrO_2 nanostructured coatings, XRD analysis with a Cu-K_α X-ray tube under an applied voltage of 40 kV was used for phase characterization of the deposited coatings. Note that the designed XRD analysis parameters were as follows: step time = 2 s, step size = 0.01°, and 2θ = 0°–100°.

The surface morphology and thickness of the Ni–P and Ni–P–ZrO_2 nanostructured coatings were analyzed by visual analysis of images obtained using FE-SEM, Gemini 500 model made by Zeiss in Germany. The electrochemical behavior of the coated samples in 3.5wt% NaCl solution was evaluated using cyclic-static polarization tests and electrochemical impedance spectroscopy. The hardness of the

deposited coatings was determined using a Vickers microhardness measurement machine with diamond impregnation under an applied load of 50 g on the cross-sectional area of the coatings. The tribological properties of the coatings were evaluated according to the stubble on the disk abrasion test using a tribometer machine, CSM Instruments SA of Switzerland. The sliding speed was approximately 5 cm/s and the slipping distance was approximately 500 m under the applied load of 20 N. An alumina bullet was used as an abrasive pair to eliminate the effects of galvanic corrosion on the abrasion test. Tribocorrosion experiments were also conducted using the back-and-forth method under alumina spheroidal abrasion in the tribometer, CETR model of the UMT-2, United States connected to the potentiostat/galvanostat, EG & G model. In the electrochemical tests, the sample was placed in a cell containing 3.5wt% NaCl solution at an anodic and cathodic potential of ± 100 mV to the open circuit potential. The back-and-forth wear test was conducted in tribocorrosion test at speed of 0.5 cm/s and under an applied load of 20 N. The three-electrode cells used in this study included an Ag/AgCl reference electrode, a platinum auxiliary electrode, and work electrodes (experimental samples). At the end of the tribocorrosion test, for the purpose of analyzing the wear mechanism in Ni–P and Ni–P–ZrO_2 nanostructured coatings, the degraded surfaces were studied using scanning electron microscopy (SEM) in a JSM-6060LV model instrument made by Japan JEOL.

3. Results and discussion

In this study, ZrO_2 nanoparticles were used as reinforcement particles in the deposited coatings. Prior to using these nanoparticles in this study, they were analyzed by TEM and XRD; the results are shown in Fig. 1. As shown in Fig. 1(a), the ZrO_2 particles used in this study have a multidimensional morphology (angular) with a mean size of 20–35 nm. The pattern of XRD analysis for ZrO_2 nanoparticles is also shown in Fig. 1(b). According to the XRD pattern shown in Fig. 1(b), the peaks of the ZrO_2 phase at the of 17.44°, 24.63°, and 50.50° angles correspond to the crystalline planes (100), (110), and (220), respectively, which is compliant with the 01-080-0966 standard card (Monoclinic, P21/c with lattice size of [a = 51.440 nm, b = 51.330 nm, and c = 53.470 nm], ICDD card #01-080-0966).

The patterns of XRD analysis for Ni–P and Ni–P–ZrO_2 nanostructured coatings that are deposited via the electroless process are shown in Figs. 2(a) and 2(b), respectively. It can be stated that the conditions of production can have a great influence on the peak intensities and the type of crystalline planes analyzed in the XRD patterns. Undoubtedly, parameters, such as the purity of the precursors, the temperature conditions of the bath, the process time, the operating conditions of sintering after deposition (if present), and the sedimentation rate, are very important. In fact, these are production conditions that determine the crystalline texture, the preferable growth orientation in the crystalline planes, and the synthesized powders size. The obtained XRD patterns in this study are in accordance with the standard cards. As shown in Fig. 2(a), the diffracted peaks at 44.37°, 51.60°, and 76.08° correspond to the crystalline planes (111), (200), and (220), respectively, of the nickel structure and perfectly match with the 00-001-1258 standard card parameters. The diffracted peaks at the angles of 44.37°, 51.60°, and 76.08° are related to the face centered cubic (FCC) structure according to the XRD pattern (face centered cubic, Fm-3m with lattice size of [a = b = c = 35.400 nm], ICDD card #00-001-1258). Moreover, the XRD pattern presented in Fig. 2(a) shows that the peak of created phosphorus appears at the angle of 35.47°, which corresponds to the 01-076-1966 standard card of the crystalline plate (111) (orthorhombic, Cmca with lattice size of [a = 33.117 nm, b = 101.580 nm, c = 42.430 nm], ICDD card #00-001-1258).

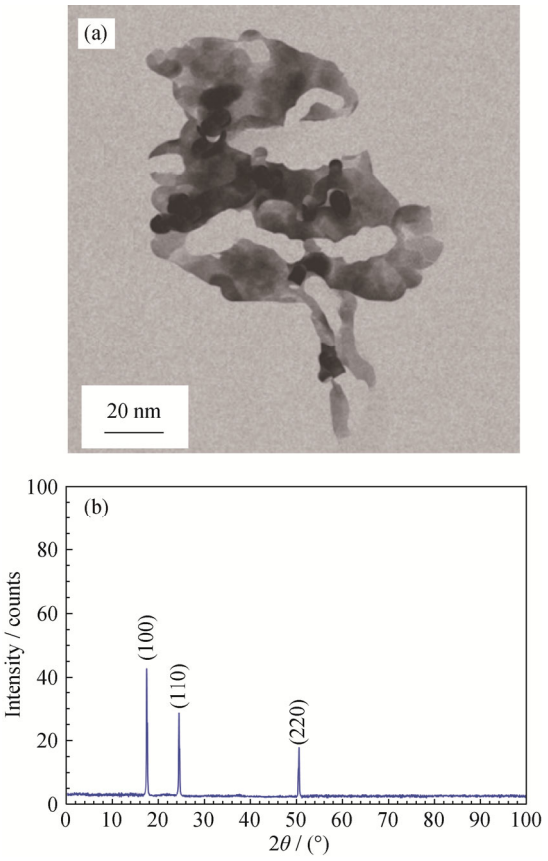

Fig. 1. Analysis of the ZrO_2 nanoparticles used in this study: (a) TEM image; (b) XRD pattern.

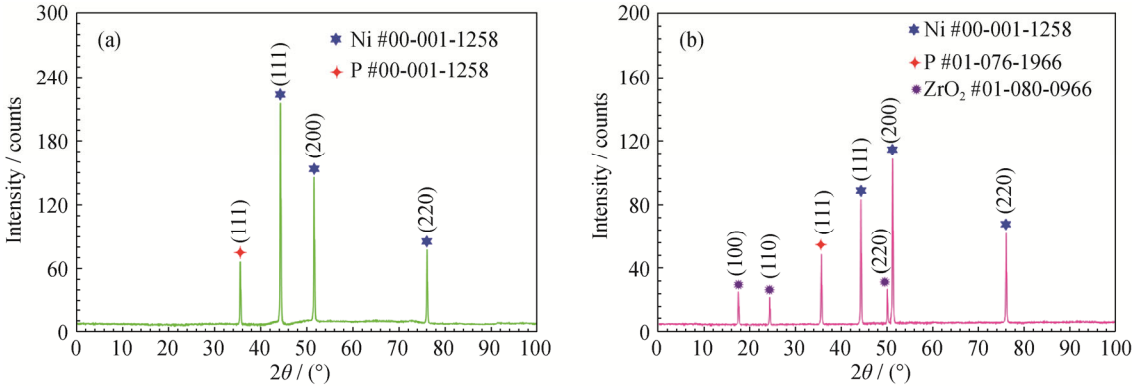

Fig. 2. XRD patterns of the coatings deposited in this study: (a) Ni–P; (b) Ni–P–ZrO_2.

The XRD pattern of the Ni–P–ZrO_2 nanostructured coating is presented in Fig. 2(b). As shown in Fig. 2(b), the diffracted peaks at the angles of 44.37°, 51.60°, and 76.08° correspond to the crystalline planes (111), (200), and (220), respectively, of the nickel structure and perfectly match with the 00-001-1258 standard card parameters. Furthermore, the peak of created phosphorus was at the angle of 35.47º, which corresponds to the angle of 01-076-1966 standard card of the crystalline plane (111). Alternatively, the peaks of the ZrO_2 phase at the angles of 17.44º, 24.63º, and 50.50º correspond to the crystalline planes (100), (110), and (220), respectively; these results are in agreement with the 01-080-0966 standard card. Note that, by comparing the XRD patterns for both Ni–P and Ni–P–ZrO_2 nanostructured coatings, the intensity of the diffracted peaks in the XRD pattern of the Ni–P–ZrO_2 nanostructured coating are observed to decrease because the absorption coefficient was altered by changing the chemical composition and structure of the deposited coating, causing a reduction in the peak intensity in the XRD pattern of the Ni–P–ZrO_2 nanostructured coating [23–24]. However, by comparing both of the XRD patterns, it is observed that adding ZrO_2 nanoparticles to the electroless bath preferentially changes the Ni growth orientation in the the Ni–P–ZrO_2 nanostructured coating. Furthermore, the higher intensity of the peak (200) indicates that the nickel present during depositing the Ni–P–ZrO_2 nanostructured coating has a tendency to grow the structure in the direction (200) relative to the direction (111). In fact, it can be stated that nickel regenerated and grew on ZrO_2 nanoparticles during the plating process of the Ni–P–ZrO_2 nanostructured coating. Therefore, new germination points (ZrO_2 nanoparticles) can change the preferential orientation of nickel growth from (111) to (200) [25–26].

The morphology, thickness, and elemental analysis of the deposited coatings in this study were investigated by FE-SEM and EDS; the results are reported in Fig. 3. Figs. 3(a) and 3(d) show the morphology of the Ni–P and Ni–P–ZrO_2 nanostructured coatings, respectively. Based on these figures, both the Ni–P nanostructured coatings and the Ni–P–ZrO_2 nanostructured coatings exhibit a spherical morphology. Previously, a number of researchers reported that the morphology of nickel-based composite coatings deposited in the chloride-based electrolyte had an anisotropic state caused by the presence of columnar and spherical beads [27–28]. In fact, this difference in morphology may be caused by the mechanism of nickel crystals growth in the electrolyte. The growth mechanism of nickel-based nanocomposite coatings is usually as follows: first, in the surface high-energy areas (such as those where the nanoparticles are deposited), nickel germination occurs in the form of spherical masses; with the continuation of the germination and growth mechanism, these nickel spherical masses grow, resulting in a structure with spherical morphology. As the number of preferred places for nickel spherical masses germination is higher, the sedimentation rate increases and, as a result, a structure is created with denser spherical morphology. Thus, by comparing the morphologies of the Ni–P and Ni–P–ZrO_2 nanostructured coatings that are shown in Figs. 3(a) and 3(d), the Ni–P–ZrO_2 nanostructured coating is found to have denser spherical morphology than the Ni–P nanostructured coating. EDS analysis was used to confirm the deposition of ZrO_2 nanoparticles in the Ni–P–ZrO_2 nanostructured coating; the results are shown in Figs. 3(c) and 3(f). The EDS results also show that the ZrO_2 nanoparticle deposition in the Ni–P field has occurred correctly.

Cross-sectional images of the Ni–P and Ni–P–ZrO_2 nanostructured coatings are shown in Figs. 3(b) and 3(e). These images show that the thickness of the coating has increased significantly by adding ZrO_2 ceramic nanoparticles to the Ni–P electroless bath. This remarkable thickness change

in the deposited nanostructured coatings can be proved by describing the germination and growth mechanisms in the electrochemical depositing systems of nanocomposite coatings. Based on Guglielmo theory, during the deposition process using the electroless plating method, ZrO_2 ceramic nanoparticles are absorbed via the electrophoresis force in appropriate locations of the surface of the globules [29]. The absorption of ZrO_2 ceramic nanoparticles leads to a change in the growth rate of the spheres; this process is called the growth site obstruction (or obstruction of the growth frontier). In this case, the sedimentation rate of the coating in the electroless bath is increased and, as a result, the thickness of the deposited coating is also increased.

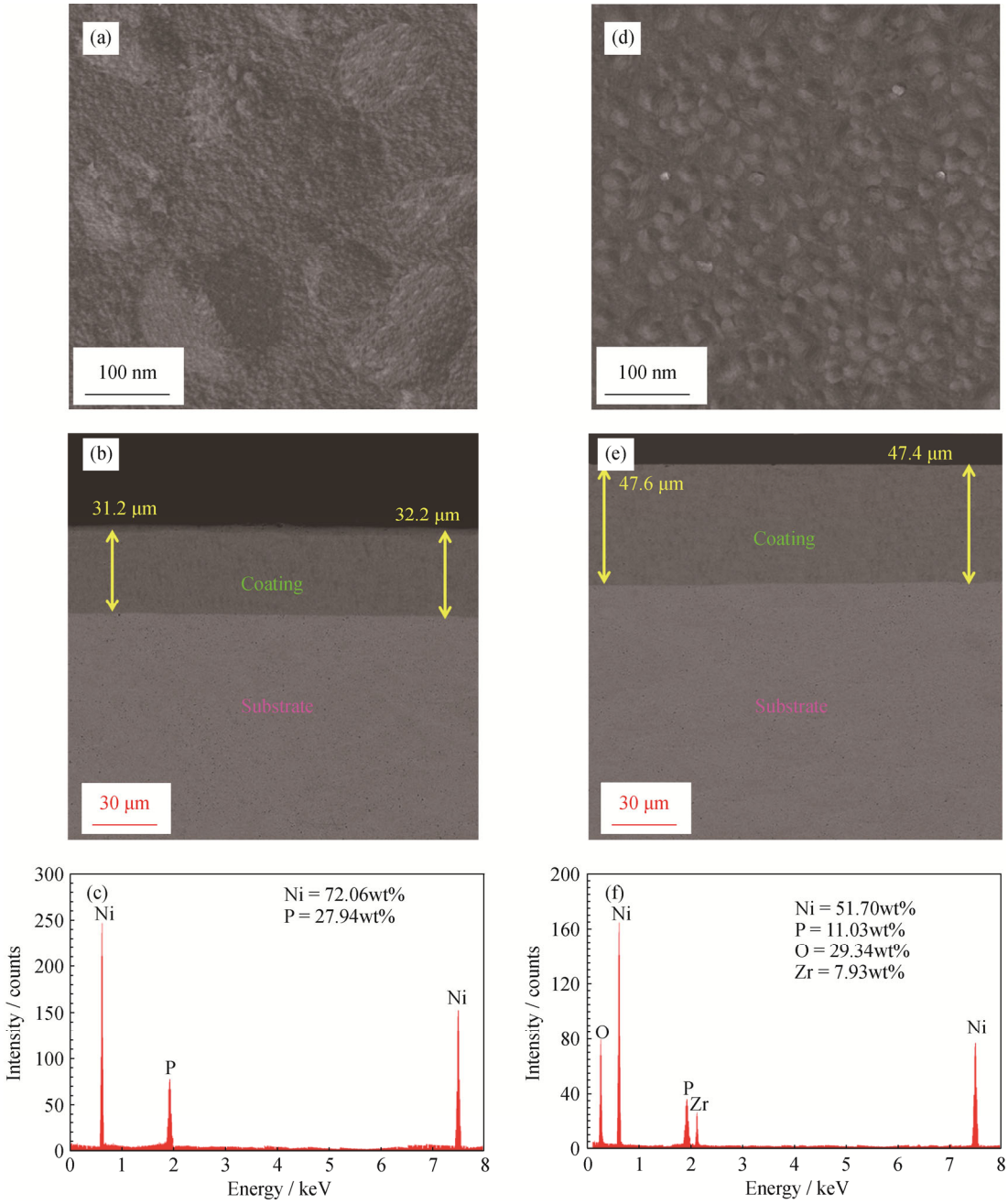

Fig. 3. FE-SEM images of the morphology and cross-section and EDS results from the coating surface: (a)–(c) Ni–P; (d)–(f) Ni–P–ZrO_2.

The cyclic polarization curves in a 3.5wt% NaCl solution for Ni–P and Ni–P–ZrO_2 nanostructured coatings are shown in Fig. 4. The presence of the passive region for both Ni–P and Ni–P–ZrO_2 nanostructured coatings is visible in the po-

larization curves. The lowest passive current density and the largest passive potential range are related to the Ni–P nanostructured coating. As shown in Fig. 4, both Ni–P and Ni–P–ZrO_2 nanostructured coatings are susceptible to pitting corrosion. Because cyclic polarization diagrams have a positive hysteresis loop, they are therefore susceptible to pitting corrosion. However, the Ni–P nanostructured coating has lower passive current density and larger passive potential range than the Ni–P–ZrO_2 nanostructured coating. The presence of a hysteresis loop in the cyclic polarization curve indicates the occurrence of pitting corrosion. The smaller the size of this loop, the greater the pitting corrosion resistance of the coating will be [30–31]. The addition of ZrO_2 ceramic nanoparticles to the Ni–P nanostructured coatings results in the formation of active/passive galvanic cells and increases the corrosion damage. In addition, with the deposition of ZrO_2 ceramic nanoparticles in the Ni–P matrix, the coating is contracted and, because of this contraction, cracks appear in the coating that can cause the electrolyte to reach the substrate and exacerbate the corrosion conditions [32–33]. According to the cyclic polarization diagrams in Fig. 4, it can be concluded that Ni–P nanostructured coatings exhibit better corrosion behavior than Ni–P–ZrO_2 nanostructured coatings because of the presence of lower residual stresses and the formation of more phosphorus in the coating. The extracted data from cyclic polarization curves are presented in Table 2. According to these data, the corrosion current density of both Ni–P and Ni–P–ZrO_2 nanostructured coatings is very low. The presence of passive-phosphate and oxide layers on Ni–P and Ni–P–ZrO_2 nanostructured coatings is one of the main factors of corrosion resistance in the open circuit potential (OCP) range for these coatings.

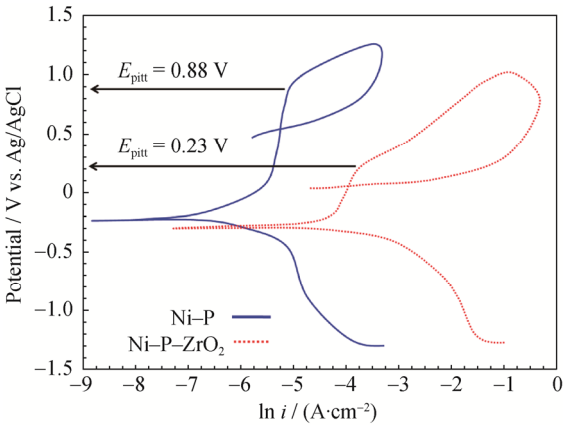

Fig. 4. Cyclic polarization diagrams for the nanostructured coatings deposited in this research.

Table 2. Extracted results from cyclic polarization diagrams

Coating	Corrosion current density / (μA·cm^{-2})	Passive current density / (μA·cm^{-2})	E_{corr} / mV vs. Ag/AgCl	E_{pitt} / mV vs. Ag/AgCl
Ni–P	1114 ± 9	5517 ± 6	−223 ± 5	884 ± 6
Ni–P–ZrO_2	11109 ± 7	22371 ± 8	−342 ± 4	234 ± 5

Note: E_{corr} is corrosion potential; E_{pitt} is pitting potential.

In this section, the tribocorrosion behavior of the deposited coatings is discussed in the OCP range. OCP variations of the deposited coatings versus immersion time are shown in Fig. 5. Immersion of the deposited coatings in 3.5wt% NaCl solution results in the formation of a passive film on the surface of the coating. With the onset of slip, the potential of the deposited coatings shifted toward higher noble potential values because of the rapid degradation of the nickel oxide passive layer and the presence of a phosphorus-rich layer in the nickel phosphate surface substrate. The corrosion potential of a phosphorus-rich layer is greater than the nickel-phosphorus coating [34–35]. Examining Fig. 5, the corrosion potential of the Ni–P nanostructured coating compared to the Ni–P–ZrO_2 nanostructured coating gradually shifts toward more noble values. Similar behavior has been observed for nickel alloy coatings [33–35]. The corrosion potential values within the range of slipping are dependent on the inherent corrosion potential of the abrasive and non-abrasive surfaces as well as the rate of repassivation of the abrasive surfaces. In fact, the ratio of active regions to passive regions determines the degree of galvanic corrosion at the abrasive surfaces and mainly affects the rate value of repassivation. Because the type of the created passive on the Ni–P and the Ni–P–ZrO_2 nanostructured coating is not identical with each other, the rate of repassivation and, consequently, the OCP variations in both coatings will be different. After finishing the slip, the Ni–P nanostructured coating is re-passivated, whereas the Ni–P–ZrO_2 nanostructured coating potential shifted to more negative values. According to the polarization diagram in Fig. 4, the reason for the negative effect of the Ni–P–ZrO_2 nanostructured coating is its tendency to localized corrosion.

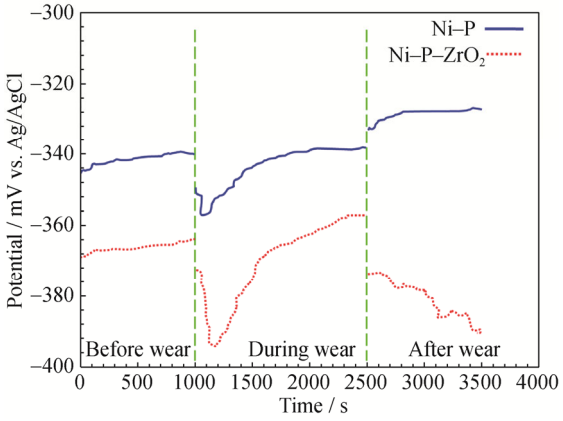

Fig. 5. OCP changes of the deposited coating in the tribocorrosion test.

In this section, the tribocorrosion behavior of the deposited coating is investigated under potentiostatic conditions. Potentiostatic tribocorrosion trials on the deposited coatings were conducted at the potential of +100 mV, which was higher than OCP for each sample in 3.5wt% NaCl solution. The data for these tests are shown in the diagrams of the corrosion current density changes versus the immersion time in Fig. 6. Immediately after immersion of the Ni–P coating in corrosive solution, nickel begins to dissolve and leads to the increase in corrosion current density. After a short time, with the formation of a passive film on the coating surface, the corrosion current density begins to decrease, and after approximately 5 min, the current value remains nearly constant. According to a report by Elsener *et al.* [36], in a Ni–P coating in chlorinated corrosive environments, the rate of nickel dissolution is higher than that of phosphorus. Therefore, a two-layer passive film that consists of a phosphate layer and a rich phosphorous layer is formed on the surface. In the Ni–P–ZrO_2 nanostructured coating, the nickel phosphate and nickel oxide films are substituted with a passive film. According to the studies of Diegle *et al.* [37], the nickel-phosphorus alloy passivation due to a surface enrichment of phosphorus is the result of the preferred dissolution of nickel. They stated that a phosphorus-rich surface reacts with water and forms a layer of hypophosphate anions ($H_2PO_2^-$). In the next step, chemical passivation blocks the flow of water to the surface of the electrode (substrate), thus preventing the hydration of nickel atoms. Nickel hydration is considered as the first step in the formation of Ni soluble species or a Ni passive film. As shown in Fig. 6, the wear has increased the current density to the positive values. The current density variations for the Ni–P nanostructured coating are relatively lower than those of the Ni–P–ZrO_2 nanostructured coating because of the tendency to rapidly form a passive form in this sample. In the case of the Ni–P–ZrO_2 nanostructured coating, much variation in the corrosion current density occurs during the wear. After the wear process, the Ni–P nanostructured coating becomes passive again and the current density returns to pre-abrasion levels. In contrast, in the Ni–P–ZrO_2 nanostructured coating, not only the current density is not diminished but also the rate of increase is far higher than the range of wear. The penetration of the corrosive solution through the cracks and coating imperfections to the substrate and the consequent corrosion of the steel substrate appears to be responsible for such behavior in the Ni–P–ZrO_2 nanostructured coating.

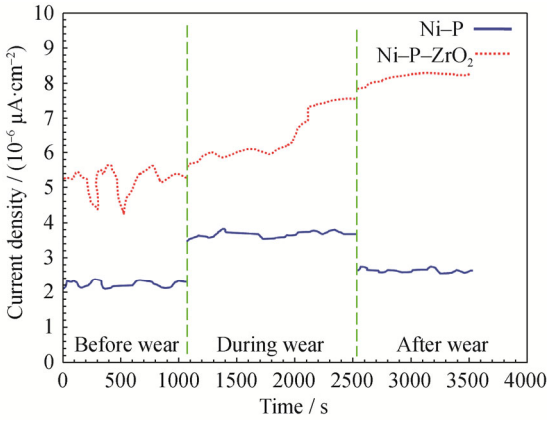

Fig. 6. Changes of the corrosion current density values for the deposited coatings at +100 mV potential versus OCP in the tribocorrosion test.

After the tribocorrosion test, the degraded surfaces were analyzed by SEM and EDS and their results are reported in Fig. 7. SEM images of the abrasive scratching point in the deposited coatings are shown in Figs. 7(a) and 7(c); the images indicate the presence of degradation caused by very slight corrosion in these coatings. In contrast, the presence of a large number of cracks and corrosion products around the abrasive scratch in the Ni–P–ZrO_2 nanostructured coating is clearly visible (Fig. 7(c)). It is also clear from these images that the addition of ZrO_2 ceramic nanoparticles to Ni–P nanostructured coatings altered the abrasion mechanism from plate-form to a laminated structure. The results of the EDS analysis of corrosion products are shown in Figs. 7(b) and 7(d). The results of the EDS analysis of corrosion products show that there are significant amounts of iron compounds in the corrosion products, indicating electrolyte penetration into the substrate and corrosion formation in the steel substrate.

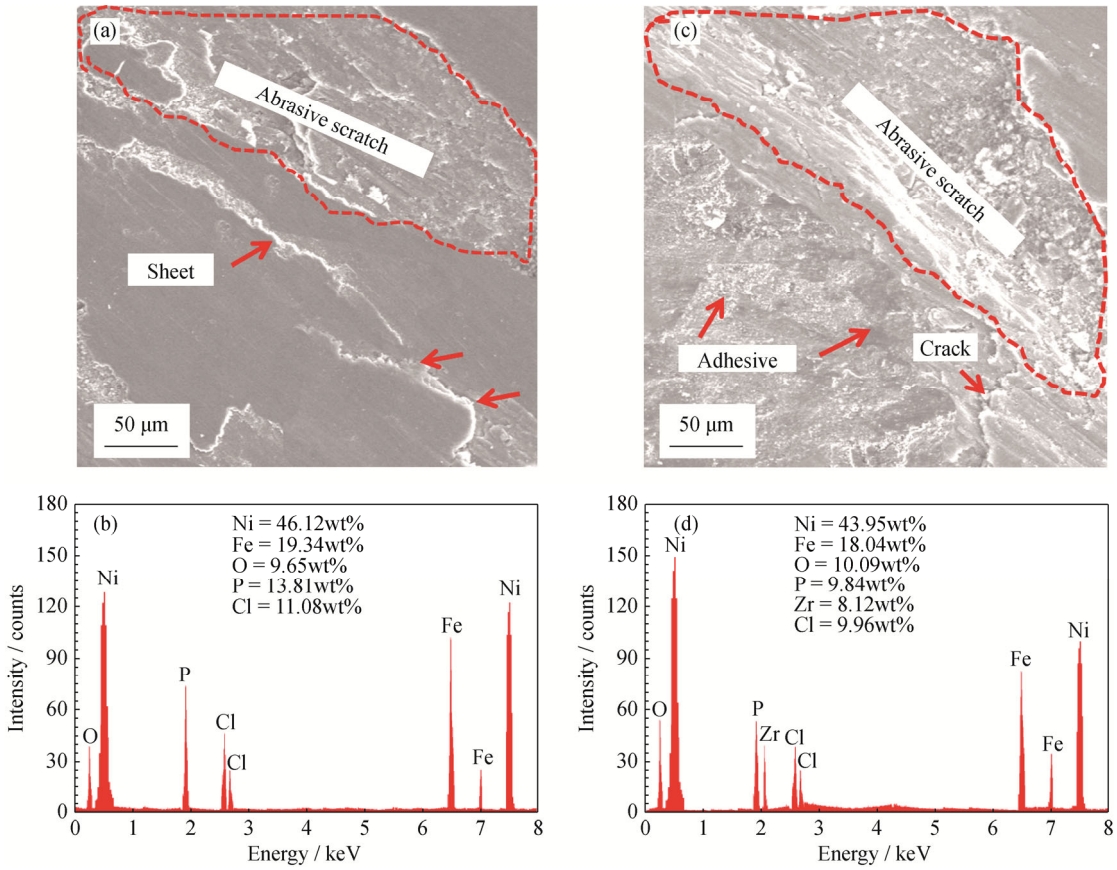

Fig. 7. EDS analysis of the corrosion products and SEM images of the scratch site for coatings after the tribocorrosion test: (a, b) Ni–P; (c, d) Ni–P–ZrO_2.

A digital scale with a precision of 10^{-4} g was used to evaluate the weight loss after the tribocorrosion test; the results are reported in Fig. 8. According to the presented diagrams in Fig. 8, the greatest value of weight loss is created in anodic potential for the tribocorrosion test. As deduced from cyclic polarization diagrams, increasing the potential to anode values increases the corrosion current density of the coatings. Therefore, according to Faraday's relationship, the amount of weight and volume loss caused by the corrosive environment will also increase. Based on this behavior, the overall weight loss is also increased at +100 mV potential relative to OCP. A similar behavior has been observed for AISI 304 steel by Sun and Rana [38]. They found that, by increasing the applied potential, the total weight dropped increased in the tribocorrosion potentiostat tests. Fig. 8 also shows that the reduced weight of the Ni–P–ZrO_2 nanostructured coating compared to the Ni–P nanostructure coating is lower in both the OCP and the anodic conditions. The higher abrasion resistance and hardness of the Ni–P–ZrO_2 nanostructures compared to the Ni–P nanostructured coating can improve its tribocorrosion behavior. Note that, although the amount of weight loss value due to tribocorrosion of the Ni–P–ZrO_2 nanostructured coating is less than the Ni–P nanostructure coating, in the used method, only the reduced weight within the wearing groove is calculated; thus, the effects of the created cracks around the groove is not considered. Accordingly, the comparison of the tribocorrosion behavior of materials in localized corrosion conditions with the consideration of the abrasive groove has limitations and disadvantages that have led researchers to modify existing methods to evaluate the material's tribocorrosion behavior.

The friction coefficient of the deposited coatings indicated during the tribocorrosion test is presented in Fig. 9. According to the results presented in Fig. 9, the friction coefficient of the Ni–P–ZrO_2 nanostructured coating is lower than that of the Ni–P nanostructured coating at both potentials. According to a report presented by DellaCorte [39], the presence of nickel oxide passive film due to good lubrication conditions reduces the friction coefficient in the Ni–P–ZrO_2 nanostructured coating. In addition, the presence of a film from nickel phosphate on the Ni–P nanostructured coating can increase the friction coefficient.

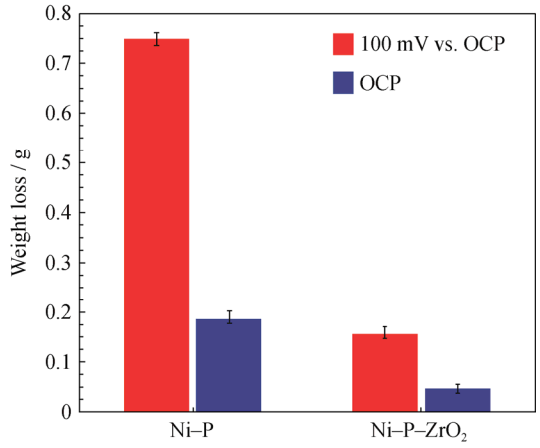

Fig. 8. Weight loss of the coatings after the tribocorrosion test at different potentials.

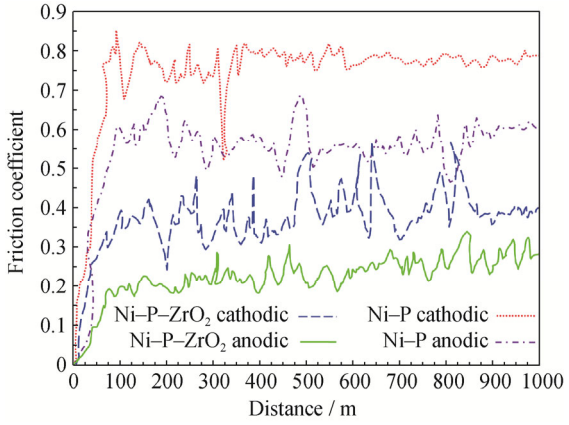

Fig. 9. Friction coefficient of the deposited coatings at different potentials.

The results of the microhardness measurement are reported in Fig. 10. Fig. 10 shows that the Ni–P–ZrO_2 nanostructured coating is harder than the Ni–P nanostructured coating. This difference is caused by the deposition of ZrO_2 ceramic nanoparticles in the Ni–P matrix. Because ZrO_2 ceramic nanoparticles have a very high hardness, they lead to an increase in the hardness of the deposited coatings. In fact, carbide and oxide particles are very hard because of the type of atomic bond [40–43]. Therefore, any change in the microstructure and chemical composition can affect the properties of the pieces [44–50].

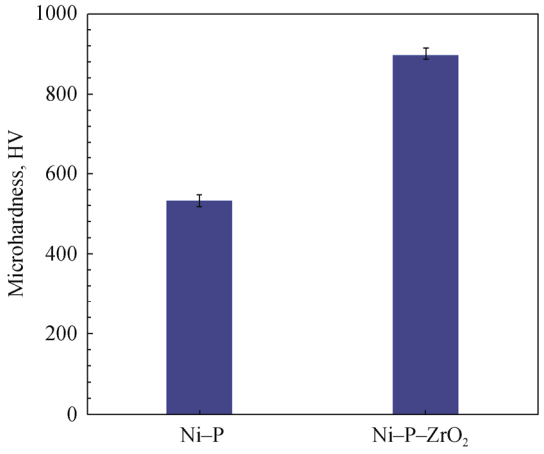

Fig. 10. Microardness of the deposited coatings.

4. Conclusions

In this study, the effect of ZrO_2 ceramic nanoparticles on the abrasive properties, crystalline texture developments, and tribocorrosion behavior of Ni–P nanostructured coatings was investigated. For this purpose, Ni–P and Ni–P–ZrO_2 nanostructured coatings were deposited on St52 steel via an electroless method. TEM, FE-SEM, XRD, cyclic-static polarization tests in a 3.5wt% NaCl solution, the tribocorrosion test (by back-and-forth wear method in the electrochemical cell), and the microhardness measurement test using the Vickers method were performed for characterization and analysis of the deposited coatings. The results obtained in this study are as follows:

(1) By comparing the XRD patterns for both Ni–P and Ni–P–ZrO_2 nanostructured coatings, it was observed that the intensity of the diffracted peaks in the XRD pattern of the Ni–P–ZrO_2 nanostructured coating decreased. By comparing both of the XRD patterns, it was observed that, after adding ZrO_2 nanoparticles to the Ni–P electroless bath, the preferred orientation of Ni growth changed in the Ni–P–ZrO_2 nanostructured coating from (111) to (200).

(2) FE-SEM images showed that both Ni–P and Ni–P–ZrO_2 nanostructured coatings have spherical morphology. By comparing the morphology of the deposited coatings in the same magnification, it became evident that the Ni–P–ZrO_2 nanostructured coating had spherical and more compact morphology than the Ni–P nanostructured coating. Moreover, studying the cross sections of the deposited coatings in the same magnification demonstrated that the presence of ZrO_2 nanoparticles in the Ni–P electroless bath resulted in an increase in the sedimentation rate during the depositing and a sharp increase in the thickness of the Ni–P–ZrO_2 nanostructured coating.

(3) The cyclic polarization curves for Ni–P and Ni–P–ZrO_2 nanostructured coatings indicated that both of the deposited coatings in the 3.5wt% NaCl solution became passive. Furthermore, the Ni–P–ZrO_2 nanostructured coating was found to exhibit higher sensitivity to localized corrosion than the Ni–P nanostructured coating.

(4) The minimum weight loss value after the tribocorrosion test in open and anodic circuit potentials was obtained

for the nanostructured Ni–P–ZrO_2 coating. The presence of ZrO_2 nanoparticles in the Ni–P–ZrO_2 nanostructured coating compared to Ni–P nanostructured coating, as well as the noble potential of ZrO_2 nanoparticles, can cause the decrease the tribocorrosion protective properties of this coating.

(5) The friction coefficient of the Ni–P–ZrO_2 nanostructured coating in the open and anodic circuit potential was lower than that of the Ni–P nanostructure coating; this observation can be attributed to the presence of a nickel oxide lubricant film and the presence of ZrO_2 nanoparticles within the nanostructured Ni–P–ZrO_2 coating.

References

[1] S.H.M. Anijdan, M. Sabzi, M.R. Zadeh, and M. Farzam, The effect of electroless bath parameters and heat treatment on the properties of Ni–P and Ni–P–Cu composite coatings, *Mater. Res.*, 21(2018), No. 2, p. 1.

[2] M. Sabzi, S.H.M. Anijdan, M.R. Zadeh, and M. Farzam, The effect of heat treatment on corrosion behaviour of Ni–P–3 gr/lit Cu nano-composite coating, *Can. Metall. Q.*, 57(2018), No. 3, p. 350.

[3] M. Sabzi, S.H.M. Anijdan, and M. Asadian, The effect of substrate temperature on microstructural evolution and hardenability of tungsten carbide coating in hot filament chemical vapor deposition, *Int. J. Appl. Ceram. Technol.*, 15(2018), No. 6, p. 1350.

[4] M. Sabzi, S.M. Far, and S.M Dezfuli, Characterization of bioactivity behavior and corrosion responses of hydroxyapatite–ZnO nanostructured coating deposited on NiTi shape memory alloy, *Ceram. Int.*, 44(2018), No. 17, p. 21395.

[5] S.H.M. Anijdan and M. Sabzi, The evolution of microstructure of an high Ni HSLA X100 forged steel slab by thermo-mechanical controlled processing, [in] *TMS 2018 147th Annual Meeting & Exhibition Supplemental Proceedings*, 2018, p. 145.

[6] S.H.M. Anijdan, M. Sabzi, M.R. Zadeh, and M. Farzam, The influence of pH, rotating speed and Cu content reinforcement nano-particles on wear/corrosion response of Ni–P–Cu nano-composite coatings, *Tribol. Int.*, 127(2018), p. 108.

[7] K. Zielińska, A. Stankiewicz, and I. Szczygieł, Electroless deposition of Ni–P–nano-ZrO_2 composite coatings in the presence of various types of surfactants, *J. Colloid Interface Sci.*, 377(2012), No. 1, p. 362.

[8] C. Gao, L. Dai, W. Meng, Z.G. He, and L. Wang, Electrochemically promoted electroless nickel–phosphorous plating on titanium substrate, *Appl. Surf. Sci.*, 392(2017), p. 912.

[9] X. Shu, Y.X. Wang, C.M. Liu, A. Aljaafari, and W. Gao, Double-layered Ni–P/Ni–P–ZrO_2 electroless coatings on AZ31 magnesium alloy with improved corrosion resistance, *Surf. Coat. Technol.*, 261(2015), p. 161.

[10] C. Hodge and M.M. Stack, Tribo-corrosion mechanisms of stainless steel in soft drinks, *Wear*, 270(2010), No. 1-2, p. 104.

[11] M. Sabzi and S.M. Dezfuli, Post weld heat treatment of hypereutectoid hadfield steel: characterization and control of microstructure, phase equilibrium, mechanical properties and fracture mode of welding joint, *J. Manuf. Processes*, 34(2018), p. 313.

[12] M. Sabzi and S.M. Dezfuli, Drastic improvement in mechanical properties and weldability of 316L stainless steel weld joints by using electromagnetic vibration during GTAW process, *J. Manuf. Processes*, 33(2018), p. 74.

[13] S.H.M. Anijdan, M. Sabzi, M. Ghobeiti-Hasab, and A. Roshan-Ghiyas, Optimization of spot welding process parameters in dissimilar joint of dual phase steel DP600 and AISI 304 stainless steel to achieve the highest level of shear-tensile strength, *Mater. Sci. Eng. A*, 726(2018), p. 120.

[14] M.C. Turk, M.J. Walters, and D. Roy, Tribo-electrochemical investigation of a slurry composition to reduce dissolution and galvanic corrosion during chemical mechanical planarization of Cu–Ru interconnects, *Mater. Chem. Phys.*, 201(2017), p. 271.

[15] M.M. Stack, W. Huang, G. Wang, and C. Hodge, Some views on the construction of bio-tribo-corrosion maps for Titanium alloys in Hank's solution: Particle concentration and applied loads effects, *Tribol. Int.*, 44(2011), No. 12, p. 1827.

[16] A.V. Kobets and T.N. Vorobyova, Palladium catalyst synthesis through sol-gel processing for electroless nickel deposition on glass, *Thin Solid Films*, 616(2016), p. 793.

[17] V. Ezhilselvi, J.N. Balaraju, and S. Subramanian, Chromate and HF free pretreatment for MAO/electroless nickel coating on AZ31B magnesium alloy, *Surf. Coat. Technol.*, 325(2017), p. 270.

[18] F. Liao, X.R. Han, Y.F. Zhang, C.J. Xu, and H.Y. Chen, Carbon fabrics coated with nickel film through alkaline electroless plating technique, *Mater. Lett.*, 205(2017), p. 165.

[19] Z.C. Shao, Z.Q. Cai, R. Hu, and S.Q. Wei, The study of electroless nickel plating directly on magnesium alloy, *Surf. Coat. Technol.*, 249(2014), p. 42.

[20] D. Li, F. Chen, Z.H. Xie, S.Y. Shan, and C.J. Zhong, Enhancing structure integrity and corrosion resistance of Mg alloy by a two-step deposition to avoid F ions etching to nano-SiO_2 reinforcement, *J. Alloys Compd.*, 705(2017), p. 70.

[21] Z.W. Song, Z.H. Xie, L.F. Ding, and Y.K. Zhang, Corrosion resistance of super-hydrophobic coating on AZ31B Mg alloy, *Int. J. Electrochem. Sci.*, 13(2018), p. 6190.

[22] R. Hu, Y.Y. Su, and H.D. Liu, Deposition behaviour of nickel phosphorus coating on magnesium alloy in a weak corrosive electroless nickel plating bath, *J. Alloys Compd.*, 658(2016), p. 555.

[23] R. Kullaiah, L. Elias, and A.C. Hegde, Effect of TiO_2 nanoparticles on hydrogen evolution reaction activity of Ni coatings, *Int. J. Miner. Metall. Mater.*, 25(2018), No. 4, p. 472.

[24] S. Arulvel, A. Elayaperumal, and M.S. Jagatheeshwaran, Electroless nickel–phosphorus coating on crab shell particles and its characterization, *J. Solid State Chem.*, 248(2017), p. 87.

[25] L.P. Wu, Z.D. Yang, and G.W. Qin, Kinetic study of a novel electroless NiP deposition on AZ91D magnesium alloy using nickel hypophosphite as the metal salt, *J. Alloys Compd.*, 694(2017), p. 1133.

[26] H. Zhao and Y.X. Lu, Comparative study of electroless nickel film on different organic acids modified cuprammonium fabric (CF), *Appl. Surf. Sci.*, 362(2016), p. 154.

[27] L.Y. Li, N. Takahashi, K. Kaneko, T. Shimizu, and T. Takarada, A novel method for nickel recovery and phosphorus removal from spent electroless nickel-plating solution, *Sep. Purif. Technol.*, 147(2015), p. 237.

[28] L. Bonin, V. Vitry, and F. Delaunois, Corrosion behaviour of electroless high boron-mid phosphorous nickel duplex coatings in the as-plated and heat-treated states in NaCl, H_2SO_4, NaOH and Na_2SO_4 media, *Mater. Chem. Phys.*, 208(2018), p. 77.

[29] N. Guglielmi, Kinetics of the deposition of inert particles from electrolytic baths, *J. Electrochem. Soc.*, 119(1972), No. 8, p. 1009.

[30] M. Sabzi, A. Obeydavi, and S.H.M. Anijdan, The effect of joint shape geometry on the microstructural evolution, fracture toughness, and corrosion behavior of the welded joints of a Hadfield steel, *Mech. Adv. Mater. Struct.*, 2018. https://doi.org/10.1080/15376494.2018.1430268.

[31] M. Sabzi and S.M. Dezfuli, A study on the effect of compositing silver oxide nanoparticles by carbon on the electrochemical behavior and electronic properties of zinc–silver oxide batteries, *Int. J. Appl. Ceram. Technol.*, 15(2018), No. 6, p. 1446.

[32] S.M. Dezfuli and M. Sabzi, A study on the effect of presence of CeO_2 and benzotriazole on activation of self-healing mechanism in ZrO_2 ceramic-based coating, *Int. J. Appl. Ceram. Technol.*, 15(2018), No. 5, p. 1248.

[33] L. Bonin, N. Bains, V. Vitry, and A.J. Cobley, Electroless deposition of nickel–boron coatings using low frequency ultrasonic agitation: Effect of ultrasonic frequency on the coatings, *Ultrasonics*, 77(2017), p. 61.

[34] P. Sahoo and S.K. Das, Tribology of electroless nickel coatings–A review, *Mater. Des.*, 32(2011), No. 4, p. 1760.

[35] F.J. He, Y.Z. Fang, and S.J. Jin, The study of corrosion–wear mechanism of Ni–W–P alloy, *Wear*, 311(2014), No. 1-2, p. 14.

[36] B. Elsener, M. Crobu, M.A. Scorciapino, and A. Rossi, Electroless deposited Ni–P alloys: corrosion resistance mechanism, *J. Appl. Electrochem*, 38(2008), No. 7, p. 1053.

[37] R.B. Diegle, N.R. Sorensen, C.R. Clayton, M.A. Helfand, and Y.C. Yu, An XPS investigation into the passivity of an amorphous Ni–20P alloy, *J. Electrochem. Soc.*, 135(1988), No. 5, p. 1085.

[38] Y. Sun and V. Rana, Tribocorrosion behaviour of AISI 304 stainless steel in 0.5M NaCl solution, *Mater. Chem. Phys.*, 129(2011), No. 1-2, p. 138.

[39] C. DellaCorte, The effect of counterface on the tribological performance of a high temperature solid lubricant composite from 25 to 650°C, *Surf. Coat. Technol.*, 86-87(1996), p. 486.

[40] S.H.M. Anijdan, and M. Sabzi, The effect of pouring temperature and surface angle of vortex casting on microstructural changes and mechanical properties of 7050Al–3wt%SiC composite, *Mater. Sci. Eng. A*, 737(2018), p. 230.

[41] S.H.M. Anijdan and M. Sabzi, The effect of heat treatment process parameters on mechanical properties, precipitation, fatigue life, and fracture mode of an austenitic Mn Hadfield steel, *J. Mater. Eng. Perform.*, 27(2018), No. 10, p. 5246.

[42] M. Sabzi, S.M. Dezfuli, and S.M. Far, Deposition of Ni–tungsten carbide nanocomposite coating by TIG welding: Characterization and control of microstructure and wear/corrosion responses, *Ceram. Int*, 44(2018), No. 18, p. 22816.

[43] S.H.M. Anijdan, M. Sabzi, M. Asadian, and H.R. Jafarian, Effect of sub-layer temperature during HFCVD process on morphology and corrosion behavior of tungsten carbide coating, *Int. J. Appl. Ceram. Technol.*, 16(2019), No. 1, p. 243.

[44] M. Sabzi, S.M. Dezfuli, and S.M. Mirsaeidghazi, The effect of pulse-reverse electroplating bath temperature on the wear/corrosion response of Ni–Co/tungsten carbide nanocomposite coating during layer deposition, *Ceram. Int.*, 44(2018), No. 16, p. 19492.

[45] S.M. Dezfuli and M. Sabzi, Effect of yttria and benzotriazole doping on wear/corrosion responses of alumina-based nanostructured film, *Ceram. Int.*, 44(2018), No. 16, p. 20245.

[46] M. Sabzi and S.M. Dezfuli, Deposition of Al_2O_3 ceramic film on copper-based heterostructured coatings by aluminizing process: Study of the electrochemical responses and corrosion mechanism of the coating, *Int. J. Appl. Ceram. Technol.*, 16(2019), No. 1, p. 195.

[47] M. Sabzi, S.H.M. Anijdan, M. Ghobeiti-Hasab, and M. Fatemi-Mehr, Sintering variables optimization, microstructural evolution and physical properties enhancement of nano-WC ceramics, *J. Alloys Compd.*, 766(2018), p. 672.

[48] M. Sabzi, S.M. Far, and S.M. Dezfuli, Effect of melting temperature on microstructural evolutions, behavior and corrosion morphology of Hadfield austenitic manganese steel in the casting process, *Int. J. Miner. Metall. Mater.*, 25(2018), No. 12, p.1431.

[49] M. Sabzi and S.H.M. Anijdan, Microstructural analysis and optical properties evaluation of sol-gel heterostructured NiO–TiO_2 films used for solar panels, *Ceram. Int.*, 45(2019), No. 3, p. 3250.

[50] M. Sabzi, A. Kianpour-Barjoie, M. Ghobeiti-Hasab, and S.M. Dezfuli, Effect of high-frequency electric resistance welding (HF-ERW) parameters on metallurgical transformations and tensile properties of API X52 microalloy steel welding joint, *Arch. Metall. Mater*, 63(2018), No. 4, p. 1693.